

IAC-16-B4.4.3,x31978

DESIGN AND TESTING OF A DUAL-CAMERA PAYLOAD FOR ESEO

Indrek Sünter

Tartu Observatory, Estonia, indrek.sunter@to.ee
University of Tartu, Estonia, indrek.sunter@estcube.eu

Henri Kuuste

Tartu Observatory, Estonia, henri.kuuste@to.ee
University of Tartu, Estonia, henri.kuuste@estcube.eu

Andris Slavinskis

Tartu Observatory, Estonia, andris.slavinskis@to.ee

Ants Agu

Estonian University of Life Sciences, Estonia, ants.agu@estcube.eu

Erik Ilbis

University of Tartu, Estonia, erik.ilbis@estcube.eu

Georgi Olentšenko

KTH Royal Institute of Technology, Sweden, georgi.olentsenko@ee.kth.se

Iaroslav Iakubivskyi

University of Tartu, Estonia, iaroslav.iakubivskyi@estcube.eu

Jacob Luis López Seco

University of Vigo, Spain, jllopseco@gmail.com

Johan Kütt

Tartu Observatory, Estonia, johan.kutt@to.ee

Riho Vendt

Tartu Observatory, Estonia, riho.vendt@to.ee

Sharad Chopra

University of Petroleum and Energy Studies, India, sharad.chopra@estcube.eu

Tõnis Eenmäe

Tartu Observatory, Estonia, tonis.eenmae@to.ee

Viljo Allik

Tartu Observatory, Estonia, viljo.allik@to.ee

Mart Noorma

University of Tartu, Estonia, mart.noorma@ut.ee

This paper presents the preliminary results of structural and electrical testing of a lightweight and power-efficient dual-camera system for European Student Earth Orbiter (ESEO). ESEO is an educational micro-satellite for monitoring the radiation environment and taking images of Earth in Low Earth Orbit (LEO) at the planned altitude of 520 km. The payload consists of a wide angle and a telescopic camera module. The wide angle camera has a 4.4 mm telecentric lens and a VGA CMOS color sensor, yielding a ground resolution of around 700 m per pixel. The telescopic camera has a Zeiss C Sonnar T* 1.5/50 lens with 50 mm focal length and a 2592 × 1944 pixel CMOS color sensor, which provides the ground resolution of about 25 m per pixel. Both cameras have a 700 nm IR cut-off filter. The resulting payload weighs about 800 g, on average consumes less than 620 mW of power, with peaks up to 1.45 W. The payload has been manufactured and is currently being tested.

I. INTRODUCTION

ESEO is a microsatellite to measure the radiation environment in LEO, test new technologies in space and take photos of Earth.¹ The aim of the ESEO optical payload is to produce color images in the visible spectrum, mainly for public outreach purposes. The proposed design consists of two visible spectrum cameras: a wide-angle camera from ESTCube-1² and an experimental telescopic camera for improved ground resolution. ESTCube-1 camera performed well throughout the two-year lifetime of the nanosatellite, delivering about 300 photos in total.³ Although the ESTCube-1 camera would already fulfil the ESEO imaging requirements, the experimental camera was included in the design to improve upon imaging resolution and test new technologies for upcoming nano- and microsatellite missions. Similar cameras have been used for proximity operations,⁴ monitoring of north arctic ice,⁵ disaster monitoring,⁶ and public outreach.^{7,8} For ESEO, the two-camera solution enables imaging of the same target with a different field of view. The wide angle image provides context for the telescopic image.

The payload has been manufactured and preliminary tests have been performed to verify that it is compatible with the ESEO bus and applicable for integration tests. While additional testing and in-depth optics characterisation is still underway, this paper presents the results of the preliminary structural and electrical tests on the ESEO camera modules.

II. DESIGN

The payload consists of two camera modules: the primary camera which is based on the ESTCube-1 camera design,² and the secondary camera, which is a new design without flight heritage. The structure of the primary camera mainly consists of a slightly modified ESTCube-1 camera structure and a box around the camera and its electronics. The secondary camera structure is designed around the optics and optimized for low mass while maintaining the structural stiffness needed against vibration. Both cameras have baffles to attenuate stray light but neither of the cameras have mechanical shutters. Instead, the integrated electronic shutters are used for both cameras. In general, the structure has been milled from aluminum, with most of the details anodized to black to reduce reflections.

The optics design of the primary camera is based

on Edmund Optics NT57-908 with 4.4 mm focal length, F/1.85 aperture and a depth of field from 0.4 m to ∞ . With the Aptina MT9V011 1/4" CMOS VGA color sensor, the primary camera has the angular resolution of 262 arcseconds per pixel and a field of view of $46^\circ \times 35^\circ$. The optics of the secondary camera are based on a modified Zeiss C Sonnar T* 1.5/50 lens with a focal length of 50 mm and an Aptina MT9P031 1/2.5" CMOS color sensor with 2592×1944 pixels. The secondary camera has an angular resolution of 9.1 arcseconds per pixel and a field of view of roughly $6.6^\circ \times 4.9^\circ$. The same 700 nm IR cutoff filter is used on both primary and secondary camera. Prior to launch, both cameras are focused to infinity.

The primary camera module hosts the power supply for both cameras, and the connectors for power and CAN bus. The cameras are interconnected with a cable which powers the secondary camera and provides CAN bus connectivity. The payload configuration is shown in figure 1. Due to the simplicity of the primary camera design, it does not feature on-board non-volatile storage of images. Acquired images are transferred to the secondary camera, which contains four SD cards. With the cameras acting as two separate payloads, it is possible to power on and communicate with each camera individually. Both camera modules run firmware that is based on the combined firmware of the ESTCube-1 camera and on-board computer.



Fig. 1: The optical payload configuration during testing.

For comparison, simultaneous images were taken with the primary (PPL) and secondary (SPL) cameras. The imaging configuration was the following: sensor gain of 2 for all channels and an exposure of 1/6000 s. The images are shown in figure 6. The secondary payload image, figure 6b, has been superimposed and highlighted with a white rectangle on the primary image, figure 6a. Iden-

tical post-processing has been performed on both images. At identical exposures times, the primary payload produces brighter images with less thermal noise thanks to larger pixel size. However, with a 12-bit color depth, the secondary payload has a wider dynamic range.⁹

III. TESTING

In order to verify that the payload would withstand launch vibrations, sine wave and random vibration tests have been performed. Spurious conducted and radiated emissions have been measured to make sure that the cameras would not interfere with other payloads or satellite bus. In addition, the cameras must be able to cope with the interference that other payloads might produce. This is typically tested with conducted and radiated susceptibility tests. As ESEO cameras shall be in a dedicated payload compartment which shields against radiated emissions, the conducted susceptibility tests were of higher priority. Compliance to ESEO electrical power system was tested with power consumption and inrush measurements at various operating temperatures and supply voltages. The payload does not have isolated CAN transceivers, due to which ripple on DC-DC output had to be measured at different loads and an over-voltage protection circuit had to be introduced into the design. In the case that the DC-DC converter failed with over-voltage on its output, the circuit would prevent the failure from propagating to satellite bus via CAN bus lines.

Communication between the payload and test engineer's laptop is enabled either via USB directly or via custom CAN to USB adapter "CANPirate".

III.i Vibration tests

For vibration tests, each camera is fastened to the vibration bench by the means of an adapter. The vibration response spectrum of the adapter, adapter with primary camera, and adapter with secondary camera were characterised before and after the test. This helped to identify fixture resonances. Both cameras were tested against sine wave (5...100) Hz at 16 g (157 m/s^2) and random vibration (5...2000) Hz at 17.38 g (170 m/s^2) on three axis.

Figures 2 and 3 show the frequency response profiles of both cameras. One of the main requirements set by ESA was that the first resonant frequency of all payloads must be above 200 Hz. It can be clearly seen that this requirement is easily fulfilled by both cameras. The features below 10 Hz come from the vibration bench's own resonant

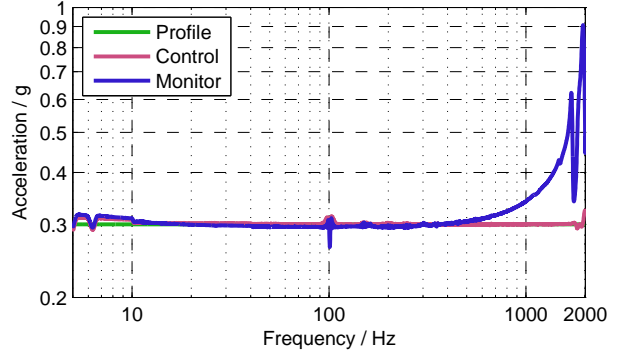


Fig. 2: PPL Vertical Axis Vibration Characterisation

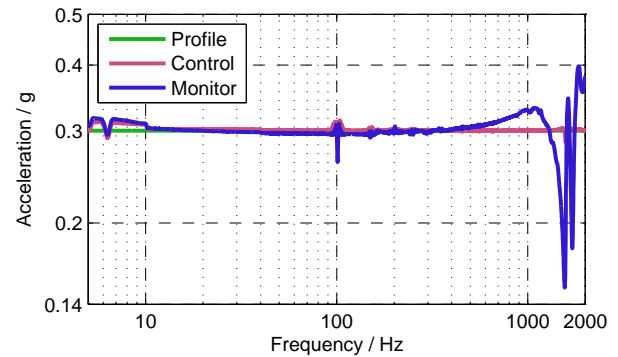


Fig. 3: SPL Vertical Axis Vibration Characterisation

frequencies. The small notch at 100 Hz as well as parts of the resonances just below 2000 Hz are caused by the camera mounting fixtures.

Each axis of the cameras was tested separately, with a simplified set of functionality tests performed in between. Although the functionality tests were all passed successfully, a few issues were identified. The secondary camera contains two SDRAM devices. The simplified set of functionality tests did not verify the second SDRAM. Following the vibration tests and thermal cycles, a via leading from the microcontroller (MCU) to the second SDRAM was found to be broken. All the other traces and vias in the vicinity of the broken via were intact. The issues caused by the broken via were intermittent in nature and might have been difficult to detect with a single run of functionality tests. Also, with vibration testing, minor tearing in material was witnessed in the baffles. In more recent designs, additional support has been added to the blades at the bottom of the baffle.

The repetitive adjustment of focus during the development of a preliminary prototype broke one of the PCB traces at the image sensor connector. The

stress on the connector was reduced in more recent designs by making the traces around the connector wider and ensuring the proper connector alignment. No issues with the connector were encountered during the vibration tests.

III.ii Power Supply Characteristics

Together with basic functionality tests, the power consumption, inrush current, voltage ripple of the payload were measured between environmental tests.

Power Consumption

The current consumption of the payload was measured during different operation mode combinations at different temperatures and supply voltages. The measurements were performed with a current transducer and an oscilloscope. Current consumption was measured at the input of a DC-DC converter with a maximum efficiency of about 70%. In addition, the measurements were taken with the USB interface enabled. Prior to launch, the USB interface would be disabled, reducing power consumption by about 100 mW.

Following the power-on of the payload, both camera modules are in idle with a total power consumption of about (610 ± 22) mW. Initializing the image sensor on the primary camera module raises the power consumption to (780 ± 20) mW for 3 s, after which the power consumption drops back to the idle levels. During the image acquisition of the primary camera, there is a peak to (778 ± 15) mW. With the primary camera switched off and the secondary camera in idle, the total power consumption is (407 ± 12) mW. With the primary camera module in idle, the initialization of the secondary camera image sensor yields a power consumption of (1198 ± 24) mW for 4 s. After the initialization, the power consumption drops back to that of idle. Image acquisition with the secondary camera produces a peak of (1391 ± 34) mW. With the primary camera in idle and the secondary camera switched off, the total power consumption is (310 ± 38) mW at which point the DC-DC converter efficiency is around 50%.

A minimum load circuit has been implemented to compensate for the unregulated output of the DC-DC converter at low loads so that the output voltage remains below 3.6 V.

A comparison of the payload power consumption in different operation modes at different temperatures and supply voltages is shown in figure 4.

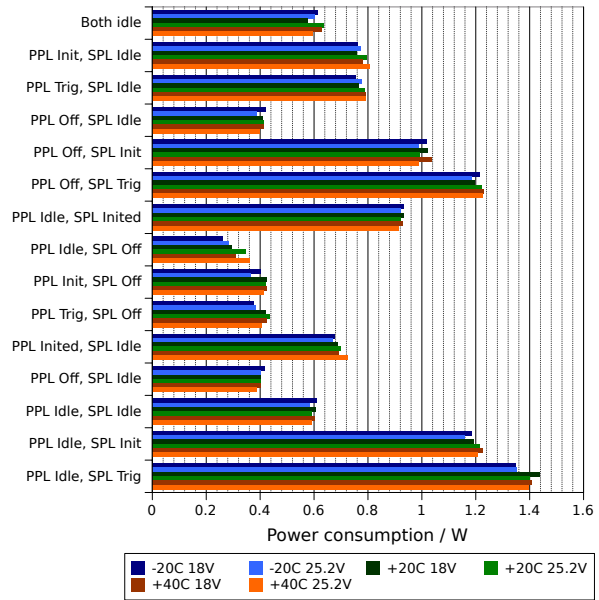


Fig. 4: Payload power consumption in different operation mode combinations at different temperatures and supply voltages.

Inrush current

In order to measure inrush current and the duration of the transient, a circuit with a bounce-free switch and a current transducer was built. The design of the bounce-free switch was based on Schmidt triggers with tactile buttons.

On average, the first peak of about 6 A appears at $14 \mu\text{s}$ since power-on, yielding an inrush current of $(325 \pm 9) \text{ mA}/\mu\text{s}$. The transient is shown in figure 5.

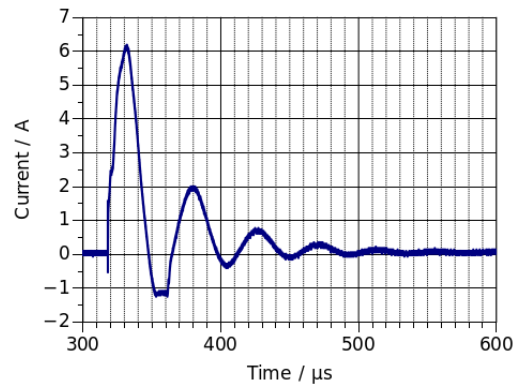


Fig. 5: Current consumption during the power-on of the payload.

Voltage ripple

Voltage ripple on the 3.3 V DC-DC converter output was measured with an oscilloscope, and found to be within 0.8% (less than 27 mV). The main ripple frequency is (173 ± 15) kHz.

Over-Voltage Protection

In the case that over-voltage would propagate from the primary to the secondary of the DC-DC converter, the payload must protect itself by cutting the power supply until the next power cycle. Another potential cause for over-voltage would be the failure of the minimum load circuit.

The over-voltage protection circuit is tested with a dedicated electronics board, which produces a short peak on the secondary of the DC-DC converter. Peak voltage and peak duration are configurable. Typically, 3.7 V for 1 ms is enough to trigger the over-voltage protection (OVP).

III.iii Electro-Magnetic Compatibility

As part of the electromagnetic compatibility (EMC) tests, conducted and radiated emissions of the payload were measured, and its susceptibility to conducted noise was tested.

Conducted Emissions

Common mode and differential mode conducted emissions tests were performed on the power and communication cables of the optical payload. The tests were initially performed at Tartu Observatory (TO), with verification measurements performed at ESTEC. Due to the lack of current probes at TO, two custom current transducers were built to cover the whole frequency range (0.3...150) kHz and (0.15...200) MHz. The tests were performed at the minimum and maximum supply voltages: 18 V and 25.2 V.

No issues were encountered with either common nor differential mode conducted emissions. The conducted emissions at the supply voltage of 18 V exceeded those of 25.2 V by up to 10 dB μ A. The comparison can be seen in figure 7. Two peaks were identified: 374.8 kHz and 1.126 MHz. While the cause of the latter peak is unclear, the former is close to the 400 kHz switching frequency of the DC-DC converter.

Radiated Emissions

Electric field radiated emissions were measured with both vertical and horizontal polarisation at both 18 V and 25.2 V supply voltages, in an anechoic chamber at TO.

A notch down to 20 dB μ V is foreseen in the limit line at the ESEO uplink frequency. At the TO EMC testing lab, the noise floor is just (1...2) dB μ V from the limit.

The initial tests revealed peaks up to 45 dB μ V on the primary and 60 dB μ V on the secondary camera. On the secondary camera, the following sources of emissions were identified (ordered by significance): uncovered connector between the image sensor and the main electronics board, and a thin gap between the structural elements surrounding the main electronics board. On the primary camera, the following sources were found: a gap between the baffle and electronics cover, and the gap in structure around the main electronics board. The required structural modifications were first tested with aluminum or copper tape. Eventually overlapping structure was implemented at the PCB edges, the contact between the PCB and the edges was improved and additional via stitching of the electronics boards was performed. This helped to reduce the peaks by (15...20) dB μ V. The background radiated emissions, and radiated emissions before and after the structural modifications are compared in figure 8. Although the emissions still intersect the uplink notch, the emissions are now acceptable due to the additional attenuation provided by the walls of the payload compartment.

Conducted Susceptibility

Common and differential mode conducted susceptibility tests were performed at ESTEC. At TO, we lacked amplifiers to cover the full frequency range of 30 Hz...100 MHz.

The payload successfully passed common and differential mode susceptibility tests on the power cable. The common mode susceptibility tests on CAN bus were aborted and differential mode measurements were not performed due to frequent loss of CAN communication with the payload. Apparently neither the custom USB-CAN adapter "CANPirate", nor the CAN bus cable reflected the flight configuration well enough. By improving the ground connections between the payload and CANPirate, the communication issues became less frequent. The CAN bus cable between CANPirate and the payload was not shielded well enough. On the other hand, differential mode susceptibility measurements would be difficult to perform on a twisted pair cable that is well shielded.

IV. CANPIRATE

CANPirate is a USB-CAN adapter based on an STM32F429I development kit with a custom shield that provides two CAN buses. The device acts as two virtual serial ports that support LAWICEL protocol,¹⁰ one for each CAN bus. CANPirate is shown in figure 9.

V. TESTING SOFTWARE

Communication with the camera modules is either performed over CAN, using the CANPirate or via USB (virtual serial port). Direct USB connection is used for transferring images, due to the limited data rate on a CAN bus with 250 kbaud. A 12-bit full frame RAW image from the secondary camera is around 8 MiB. However, the payload data rate via CAN can not exceed 2 KiB/s. The testing software must also support the 1 Mbaud RS-485 interface, to test inter-camera communication.

A dedicated terminal application "CANTerminal" has been developed to facilitate communication with the cameras via any of these interfaces. CANTerminal is developed in Python, which simplifies prototyping and makes the software easily extendable. Similarly to the camera modules, CANTerminal is based on the CanFestival¹¹ CANopen stack. Boost::Python is used to interface the CanFestival C library from Python. A screenshot of CANTerminal is shown in figure 10.

For each configured camera module, CANTerminal runs a python interpreter with a set of functions that are translated into binary commands and sent to the camera. USB command and response structures are described in XML configuration files. CAN bus communication is built upon registers, 4 B each. Since several commands expect more than 4 B of arguments, additional low-level logic is needed to map Python functions to CAN bus registers. The commands and responses for CAN communication are defined in camera-specific Python scripts which are then interpreted at runtime. A command buffer register has been implemented on the cameras, to facilitate the transmission of USB commands via CAN. Responses to these commands are stored in a dedicated file on-board each camera. Based on the configuration files, CANTerminal auto-generates documentation for the USB commands and responses. Currently the documentation for CAN bus register API is not auto-generated.

Extensions have been developed for image acquisition and analysis, color calibration, generic file

transfer, and decompression and extraction of files downloaded from the cameras. Moreover, automatic testing of imaging with support for external equipment control (such as the monochromator) has been implemented as an extension.

An extension has also been developed for the periodic monitoring of an active camera module during the EMC susceptibility tests. The cameras are set to collect housekeeping data at 2 Hz and validate the measurements against pre-configured limits. In addition, quick on-board read-write-readback tests are performed for each memory device. CANTerminal polls the results of the memory tests and housekeeping limit checks, which it then displays on a panel of indicators. The same extension is also used for the on-board detection of anomalies and noise on the camera images. A screenshot of the extension is shown in figure 11.

VI. DISCUSSIONS

The testing of the payload has been successful, however several important lessons have been learned.

Flat flex cables could be used between moving inter-board connections to reduce stresses. During vibration testing we encountered some resonances in our test setup. Our design of the vibration bench adapter consists of multiple pieces that are bolted together. However, in order to reduce resonances, it is suggested to design vibration bench adapters as monolithic pieces of aluminum.

The harness and grounding of the equipment under testing (EUT) has a major effect on the results of the EMC susceptibility tests. Thus, it is suggested to perform the tests on an integrated module that closely resembles the flight configuration. In the case of the optical payload, the tests should be performed with the cameras mounted onto the walls of the payload compartment, with flight harness. In addition, instead of a laptop communicating to the cameras, a stand-alone satellite bus simulator should be used.

Automated testing software has saved a lot of manhours of work. With the automation of all the functionality tests, the total testing time could be reduced even more. It is important to verify that the functionality tests cover all peripherals and redundant systems either between or during the environmental tests.

Susceptibility tests assume on-board software that performs all the tests and validation on-board. Moreover, the time duration of a single iteration of all the on-board tests and validation should be less than the

susceptibility test dwell time. This makes it possible to relate detected anomalies to specific frequencies.

VII. CONCLUSION

A dual-camera payload has been developed for the European Student Earth Orbiter mission. Most of the tests required for the closure of the Critical Design Review (CDR) have been performed. The identified issues have been resolved and currently the updated payload is undergoing additional testing. While the preliminary tests show that the payload is ready for integration testing, the measurements of spectral sensitivity, baffle efficiency and stability of optical alignment are still to be performed on the assembled flight model.

ACKNOWLEDGEMENTS

The development of the ESEO optical payload has been funded by ESA PECS2 (contract no. 4000107255/12/NL/SFe) and carried out by Tartu Observatory, University of Tartu and The Estonian University of Life Sciences. The authors would like to thank ProtoLab for close cooperation in the development of the camera structure, Brandner for the manufacturing of the electronics boards, ESTEC for providing the facilities for EMC testing and SITAEL for all their help and coordination.

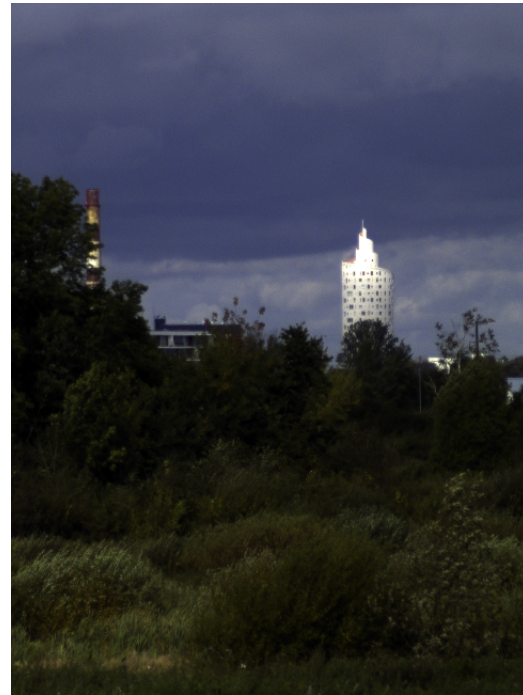
REFERENCES

- [1] Davide Bruzzi, Paolo Tortora, Fabrizio Giulietti, and Piero Galeone. European student earth orbiter: ESA's educational microsatellite program. In *AIAA/USU Conference on Small Satellites*, 2013.
- [2] Henri Kuuste, Tõnis Eenmäe, Viljo Allik, Ants Agu, Riho Vendt, Ilmar Ansko, Kaspars Laizāns, Indrek Sünter, Silver Lätt, and Mart Noorma. Imaging system for nanosatellite proximity operations. *Proc. of the Estonian Academy of Sciences*, 63:250–257, May 2014.
- [3] Silver Lätt, Andris Slavinskis, Erik Ilbis, Urmas Kvell, Kaupo Voormansik, Erik Kulu, Mihkel Pajusalu, and et al. Estcube-1 nanosatellite for electric solar wind sail in-orbit technology demonstration. *Proc. of the Estonian Academy of Sciences*, 63:200–209, May 2014.
- [4] Christopher W. T. Roscoe, Jason J. Westphal, and Robert T. MacMillan. Reusable bird's-eye view for on-orbit satellite servicing using cubesats. In *39th AAS Guidance, Navigation, and Control Conference*, 2016.
- [5] Sangkyun Kim, Takashi Eishima, Naoki Miyashita, Yuta Nojiri, and Yuya Nakamura. WNISAT - nanosatellite for north arctic routes and atmosphere monitoring. In *24th Annual AIAA/USU Conference on Small Satellites*, 2010.
- [6] Mohamed Kameche, Haider Benzeniar, Ayhane Bey Benbouzid, Redha Amri, and Nadir Bouanani. Disaster monitoring constellation using nanosatellites. *Journal of Aerospace Technology and Management*, 6:93–100, March 2014.
- [7] Jun ichi Ozaki, Tomoyuki Ikeda, Tatsuya Fujiwara, Masaya Nishizawa, Shunsuke Araki, Hirokazu Tahara, and Yosuke Watanabe. Development of osaka institute of technology nanosatellite "PROITERES" with electrothermal pulsed plasma thrusters. In *32nd International Electric Propulsion Conference*, 2011.
- [8] Mitsuhiro Komatsu and Shinichi Nakasuka. University of tokyo nano satellite project "PRISM". 2009.
- [9] Indrek Sünter, Henri Kuuste, Johan Kütt, Erik Ilbis, Ants Agu, Iaroslav Iakubivskyi, Sharad Chopra, Tavo Ani, Jacob Luis López Seco, Tõnis Eenmäe, Viljo Allik, Georgi Olentšenko, Jaanus Kalde, Samu-Pekka Ojanen, Sriram Hariharan, Allan Kustavus, Karoli Kahn, Indrek Ploom, Riho Vendt, Silver Lätt, Urmas Kvell, and Mart Noorma. Dual-camera payload for ESEO. In *The 4S Symposium 2016*, 2016.
- [10] LAWICEL. Can232 manual, 2013. http://www.can232.com/docs/can232_v3.pdf.
- [11] CanFestival. Free software CANopen framework, 2016. <http://wwwcanfestival.org>.

IMAGES



(a) Image taken with the primary camera.



(b) Image taken with the secondary camera (down-scaled 4x).

Fig. 6: Comparative image from both cameras: (a) taken with the primary (ESTCube-1) camera, and (b) taken with the secondary (experimental) camera.

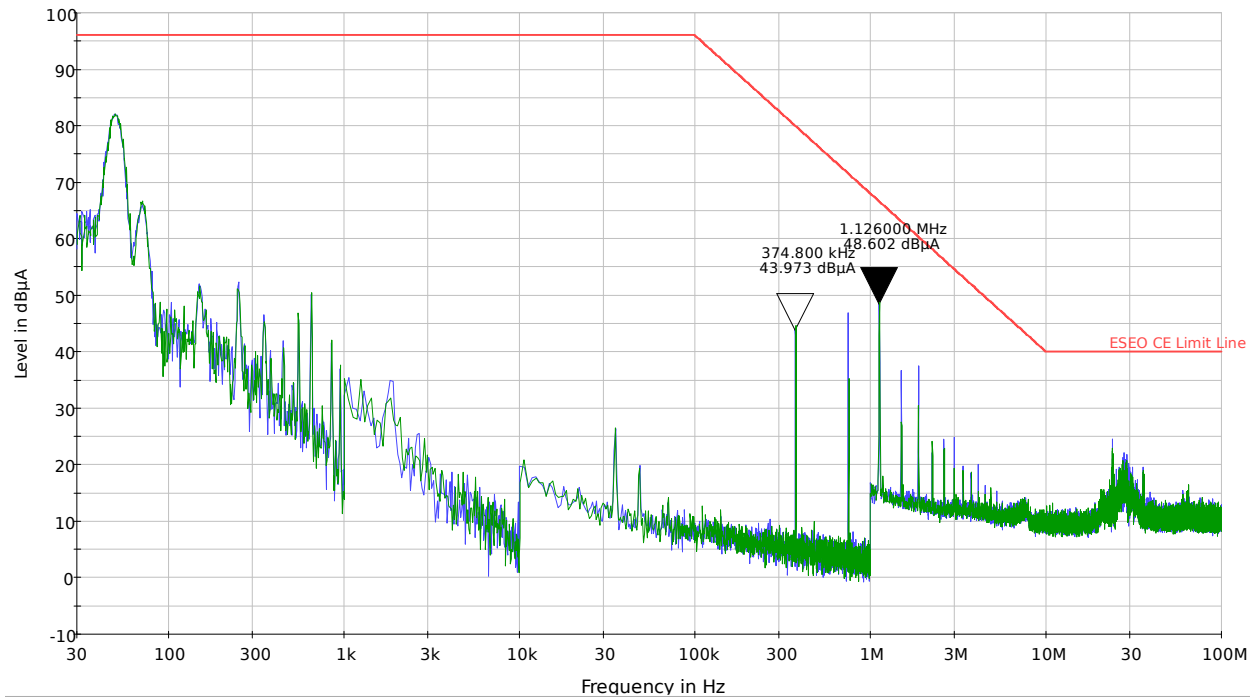


Fig. 7: Common mode conducted emissions on the power cable. Emissions at 18 V supply are shown in blue and emissions at 25 V are shown in green.

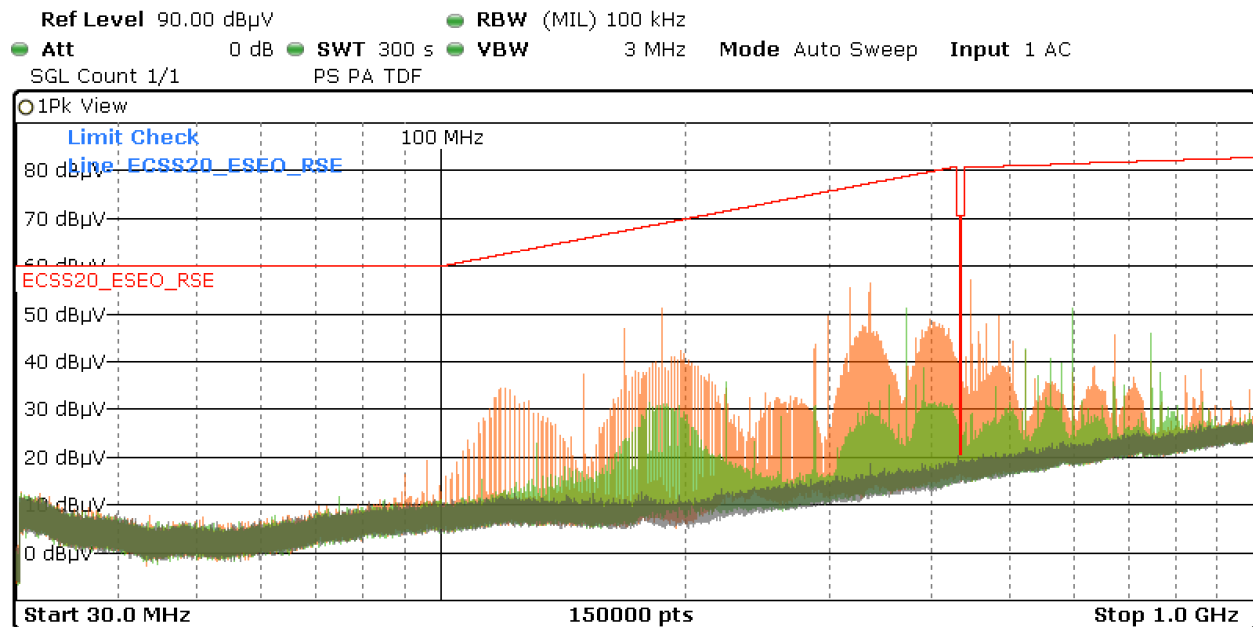


Fig. 8: Radiated emissions of the secondary camera before (orange) and after the structural modifications (green). Limit line is shown in red and measurement noise floor is shown in gray. The measurements have been performed at 25.2 V supply with vertical polarity.

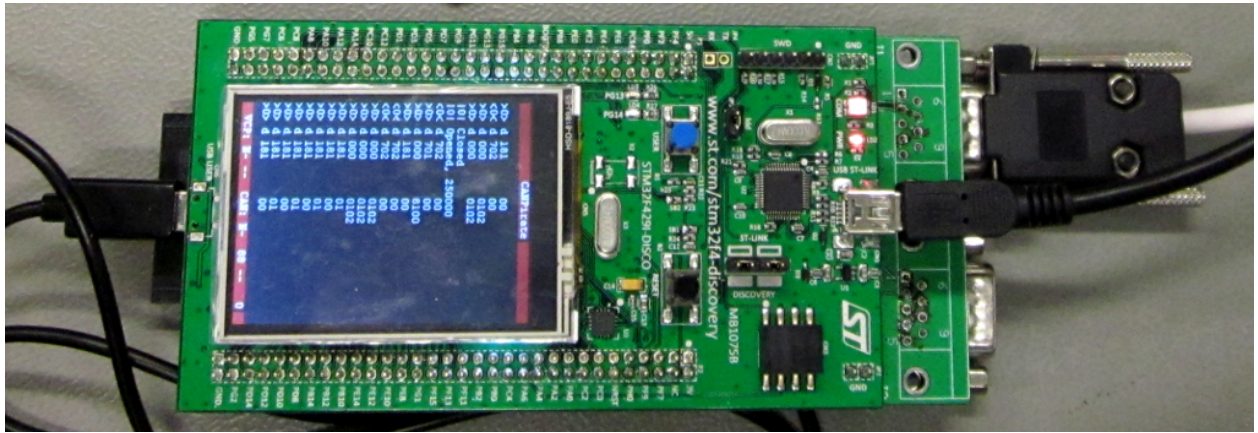


Fig. 9: CANPirate CAN bus to USB adapter.

S-CAM

Script buttons

File management

Test group

Ping

Right-click to create groups

S-CAM **P-CAM**

Noise Detection

Test Status: Unknown

Memtest initialized

Vin	S_IMG	T_RTC	I_MCU	T_MCU
RAM1	RAM2		I_RAM	T_RAM
FRAM1	FRAM2	FRAM3	FRAM4	I_IMG T_IMG
SD1	SD2	SD3	SD4	I_SD T_SD

CAN phy errors: 22 CANPirate errors: 0
CanFestival errors: 1 PyCF errors: 0

Fig. 10: CANTerminal with a terminaldock open for the secondary camera.

Fig. 11: CANTerminal extension used for susceptibility testing.